J. Fluid Mech. (2024), *vol*. 1001, R2, doi:10.1017/jfm.2024.1131

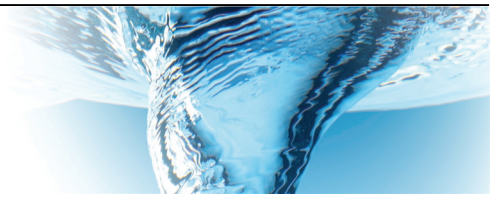

Scaling laws and mechanisms of hydrodynamic dispersion in porous media

Yang Liu[1], **Han Xiao**[1], **Tomás Aquino**[2], **Marco Dentz**[2],† **and Moran Wang**[1],†

[1]Department of Engineering Mechanics, Tsinghua University, Beijing 100084, PR China

[2]Spanish National Research Council (IDAEA-CSIC), Barcelona 08034, Spain

(Received 22 September 2024; revised 27 October 2024; accepted 19 November 2024)

We present a theory that quantifies the interplay between intrapore and interpore flow variabilities and their impact on hydrodynamic dispersion. The theory reveals that porous media with varying levels of structural disorder exhibit notable differences in interpore flow variability, characterised by the flux-weighted probability density function (PDF), $\hat{\psi}_\tau(\tau) \sim \tau^{-\theta-2}$, for advection times τ through conduits. These differences result in varying relative strengths of interpore and intrapore flow variabilities, leading to distinct scaling behaviours of the hydrodynamic dispersion coefficient D_L, normalised by the molecular diffusion coefficient D_m, with respect to the Péclet number Pe. Specifically, when $\hat{\psi}_\tau(\tau)$ exhibits a broad distribution of τ with θ in the range of $(0, 1)$, the dispersion undergoes a transition from power-law scaling, $D_L/D_m \sim Pe^{2-\theta}$, to linear scaling, $D_L/D_m \sim Pe$, and eventually to logarithmic scaling, $D_L/D_m \sim Pe\ln(Pe)$, as Pe increases. Conversely, when τ is narrowly distributed or when θ exceeds 1, dispersion consistently follows a logarithmic scaling, $D_L/D_m \sim Pe\ln(Pe)$. The power-law and linear scaling occur when interpore variability predominates over intrapore variability, while logarithmic scaling arises under the opposite condition. These theoretical predictions are supported by experimental data and network simulations across a broad spectrum of porous media.

Key words: porous media, dispersion

1. Introduction

The transport of solutes through porous media is a fundamental topic with extensive applications across various fields, including geological carbon sequestration (Huppert & Neufeld 2014), fuel cells (Peng *et al.* 2020), packed-bed reactors (Jurtz, Kraume & Wehinger 2019) and microcirculation in the human body (Goirand, Le Borgne &

† Email addresses for correspondence: marco.dentz@csic.es, moralwang@jhu.edu

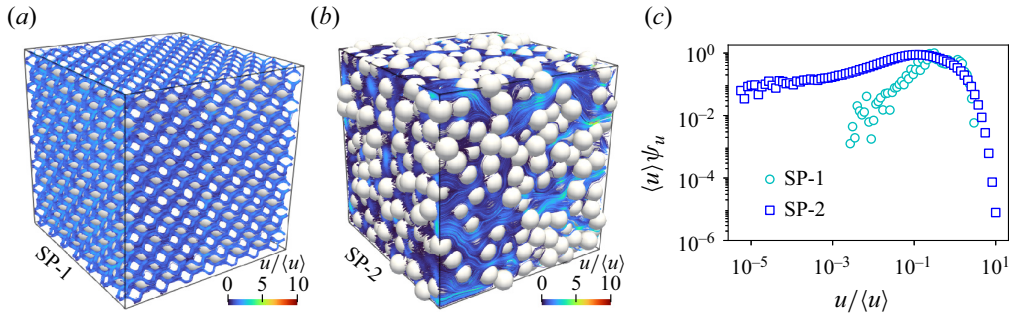

Figure 1. Streamlines through (*a*) SP-1, a regular pack of spheres, and (*b*) SP-2, a random pack of spheres. Colours render the Eulerian velocity u normalised by the mean value $\langle u \rangle$. (*c*) Probability density function (PDF) ψ_u of Eulerian velocities.

Sylvie 2021). Hydrodynamic dispersion theory quantifies solute transport by averaging variations in fluid velocity and solute concentration (Sahimi 2011; Bear 2013). Porous media flow exhibits multiscale heterogeneity, characterised by variations in flow velocities both within individual pores (intrapore) and between different pores (interpore). Intrapore flow variability can arise from two primary factors: the no-slip condition, which results in higher velocities at the pore centre and lower velocities near the walls, and the roughness of pore surfaces, which generates complex streamlines and affects solute transport within the pores significantly (Sahimi & Imdakm 1991; Bizmark *et al.* 2020). This study focuses exclusively on the impact of the no-slip condition. Interpore flow variability arises from structural disorder across pores (figure 1*b*), creating preferential flow channels and stagnant regions (Kandhai *et al.* 2002; Liu *et al.* 2024*a*). Both intrapore and interpore variabilities intensify the overall variations of porous media flow, thereby enhancing hydrodynamic dispersion.

The longitudinal dispersion coefficient, a critical parameter in dispersion theory, encapsulates the upscaling effect of the heterogeneous flow field and quantifies the porous medium's capacity to disperse solutes (Dentz, Hidalgo & Lester 2023). Experimental data from disordered porous media reveal distinct scaling behaviours between the hydrodynamic dispersion coefficient D_L and the Péclet number Pe, categorised into different regimes (Sahimi 2011; Bear 2013). In the range $10^0 < Pe < 10^3$, termed the power-law regime, there exists a power-law scaling described by $D_L/D_m \sim Pe^{\kappa}$ ($\kappa \approx 1.2$) (Sahimi 2011), where D_m denotes the molecular diffusion coefficient. For $10^3 < Pe < 10^6$, known as the convective regime, a linear scaling is observed as $D_L/D_m \sim Pe$ (Sahimi 2011).

The current understanding of the scaling behaviours between D_L and Pe remains limited. On the one hand, numerical simulations have yielded conflicting conclusions concerning the primary mechanism driving the power-law regime. Some studies (Sahimi *et al.* 1986; Sahimi & Imdakm 1988; Bijeljic, Muggeridge & Blunt 2004; Jha, Bryant & Lake 2011; Mehmani & Balhoff 2015) have emphasised the critical role of intrapore flow variability, while others (De Arcangelis *et al.* 1986; Acharya *et al.* 2007; Van Milligen & Bons 2014) observe that superlinear scaling can occur without accounting for intrapore flow variability, provided that the pore structure exhibits a certain degree of disorder. On the other hand, both experimental observations (Pfannkuch 1963; Delgado 2005; Lehoux *et al.* 2016) and numerical simulations (De Arcangelis *et al.* 1986; Maier *et al.* 2000; Bijeljic *et al.* 2004; Bijeljic & Blunt 2006; Mostaghimi, Bijeljic & Blunt 2010; Mehmani &

Balhoff 2015) show a transition from superlinear power-law to linear scaling as the Péclet number increases. However, current theoretical models (Saffman 1959; Koch & Brady 1985; Bear & Bachmat 1986; Puyguiraud, Gouze & Dentz 2021) describe the dispersion coefficient D_L as a combination of linear and superlinear terms in relation to the Péclet number Pe. These models indicate that once a superlinear growth of D_L with respect to Pe emerges, it will continue as Pe increases, without reverting to a linear relationship.

The discrepancies among studies are attributed to inconsistencies in the relative strengths of interpore and intrapore flow variabilities. These inconsistencies alter flow statistics (figure 1*c*) and, ultimately, the relationship between D_L and Pe (Bruderer & Bernabé 2001). For instance, network simulations have utilised networks with diverse structural disorder, characterised by the distribution of pore sizes (De Arcangelis *et al.* 1986; Bijeljic *et al.* 2004; Acharya *et al.* 2007) and coordination numbers (Sahimi *et al.* 1986; Jha *et al.* 2011; Mehmani & Balhoff 2015), as well as various domain sizes (Bijeljic *et al.* 2004; Jha *et al.* 2011; Mehmani & Balhoff 2015), leading to varying degrees of interpore flow variability. Theoretical models have limitations in resolving interpore (Saffman 1959; Koch & Brady 1985) or intrapore (Bear & Bachmat 1986; Puyguiraud *et al.* 2021) flow variability. Thus, the interplay between these flow variabilities and their effect on hydrodynamic dispersion remain poorly understood.

In this work, we address these fundamental issues through a stochastic model that connects structural disorder, flow variability and hydrodynamic dispersion. Our findings indicate that in porous media with diverse distributions of structural disorder, the significance of interpore flow variability on dispersion varies, thereby altering the scaling relationship between the dispersion coefficient and the Péclet number. The robustness and precision of our theoretical model are supported by experimental data and numerical simulations across a wide spectrum of porous media.

2. Theoretical model

We investigate hydrodynamic dispersion in disordered, statistically homogeneous porous media without dead-ends. The pore structure is idealised as a network of pores (junctions) interconnected by throats (bonds), a model widely utilised in studies of flow and transport in porous media (Fatt 1956; Liu *et al.* 2022, 2024*b*). Pores are assumed to have zero volume within which solutes are mixed completely. Throats are conduits with circular cross-sections, where fluid flow follows the Poiseuille law. The global Péclet number is defined as $Pe = \bar{U}\ell/D_m$. Here $\bar{U}$ denotes the average velocity, which is calculated as the Darcy velocity divided by porosity, and ℓ is the characteristic length, typically taken as the grain size.

Solute transport is modelled in the continuous time random walk (CTRW) framework (Berkowitz *et al.* 2006) through spatiotemporal transitions, where the solute mass is discretised into tracer points that follow Lagrangian trajectories. During each transition, solute tracer moves from one pore to another via a connecting throat with longitudinal displacement Δx and duration Δt. The displacement is given by $\Delta x = l\cos\beta$, where l and β denote the length of the throat and its alignment angle to the longitudinal direction, respectively. We assume that Δx and Δt are independent random variables, characterised by the probability density functions (PDFs) $\omega(x)$ and $\psi(t)$, respectively. This assumption is supported by the weak correlation in tracer velocities across pores (Bijeljic, Mostaghimi & Blunt 2011; de Anna *et al.* 2013; Dentz *et al.* 2016; Alim *et al.* 2017). Within the CTRW

framework, the longitudinal dispersion coefficient D_L is derived as

$$D_L = \frac{\langle x \rangle^2}{2\langle t \rangle} \frac{\langle t^2 \rangle - \langle t \rangle^2}{\langle t \rangle^2}, \tag{2.1}$$

$$\langle t^m \rangle = \int t^m \psi(t)\, \mathrm{d}t, \quad \langle x^m \rangle = \int x^m \omega(x)\, \mathrm{d}x, \tag{2.2a,b}$$

where $m = 1, 2$. A detailed derivation of this expression is provided in the supplementary material available at https://doi.org/10.1017/jfm.2024.1131, see also Dentz *et al.* (2004).

Equation (2.1) emphasises the critical role of $\psi(t)$ in the scaling relationships between D_L and Pe. The PDF $\psi(t)$ characterises the statistical properties of tracer transition times throughout the network and is shaped by both intrapore and interpore flow variabilities, as well as molecular diffusion. Molecular diffusion plays two primary roles: solute tracer moves across streamlines via diffusion, sampling flow velocities within the conduit; and as the slowest transport mechanism, it sets the maximum transition time as the axial diffusion time $\tau_D = l^2/D_m$.

Only a few studies (de Anna *et al.* 2017; Dentz, Icardi & Hidalgo 2018; Puyguiraud *et al.* 2021) have attempted to derive $\psi(t)$ from structural and flow properties, and these are predominantly limited to the scenario where tracer transitions are governed by advection. However, strong interpore flow variability can result in diverse modes of tracer transitions. For example, transitions may be primarily advection-dominated in preferential flow conduits while it is diffusion-dominated in others. Consequently, these studies (de Anna *et al.* 2017; Dentz *et al.* 2018; Puyguiraud *et al.* 2021) do not fully capture the characteristics of the PDF $\psi(t)$. Moreover, the relative contributions of intrapore vs interpore flow variabilities to $\psi(t)$ remain unexplored.

We first examine the impact of interpore flow variability on tracer transitions. This variability is characterised by variations in flow properties across conduits, including the flow rate q, the maximum velocity v and the advection time $\tau = l/v$. Interpore flow variability arises from the random distribution of geometrical properties of conduits, such as radius R, length l, orientation angle β and cross-sectional shape. According to the Poiseuille law, the hydraulic conductance K of a conduit, defined as the volumetric flow rate per unit pressure drop, conforms to $K \sim R^4 l^{-1}$. For homogeneous networks, it is reasonable to assume a uniform pressure gradient $G = |\nabla P|$ along the longitudinal direction. The pressure drop across the throat is given by $\Delta P = Gl\cos\beta$, leading to the following relationships: $q \sim R^4 G\cos\beta$, $v \sim R^2 G\cos\beta$ and $\tau \sim R^{-2} l (G\cos\beta)^{-1}$. It is apparent that the radius R exerts the most significant influence on interpore flow variability. Thus, we assume the conduit radii within the network are randomly distributed, while other properties, such as length, orientation and cross-sectional shape, remain constant across all conduits.

The PDF $\psi_R(R)$ of conduit radii within porous media is commonly modelled using power-law (de Anna *et al.* 2017), Weibull (Assouline, Tessier & Bruand 1998; Dentz *et al.* 2018) and Gamma (Johnston 1998) distributions. Asymptotic dispersion is shaped by smaller-sized pores, which determine the tail of $\psi(t)$ (Puyguiraud *et al.* 2021). Since Weibull and Gamma distributions behave as power laws for small values, $\psi_R(R)$ is modelled here as a power-law distribution,

$$\psi_R(R) \sim R^{\alpha}, \quad R \in [R_{min}, R_{max}], \tag{2.3}$$

where R_{min} and R_{max} represent the minimum and maximum radii, respectively. Thus, the PDF of advection times τ behaves as $\psi_\tau(\tau) \sim \tau^{-(\alpha+3)/2}$. Our model focuses on

hydrodynamic dispersion, where advection dominates on a global scale. As a result, the fraction of tracer mass entering a connecting tube at a pore node is proportional to the flow rate in that tube, an assumption adopted widely in previous studies (Sahimi *et al.* 1986; Bijeljic *et al.* 2004; Puyguiraud *et al.* 2021). In other words, tracer redistribution at pore nodes is proportional to the flux. Therefore, the PDF $\hat{\psi}_\tau(\tau)$ for tracer selecting a downstream conduit with an advection time of τ is given by the flux-weighted PDF of τ,

$$\hat{\psi}_\tau(\tau) = \frac{q}{\langle q \rangle}\psi_\tau(\tau) = C_\tau \tau^{-\theta-2}, \quad \tau \in [\tau_{min}, \tau_{max}], \tag{2.4}$$

where $\theta = (\alpha + 3)/2$ and C_τ is a normalisation constant. Here τ_{min} and τ_{max} denote the minimum and maximum advection times, respectively.

Next, we examine the influence of intrapore flow variability by analysing the advective–diffusive transport of solutes within a circular tube of radius R and length l. To this end, we consider solute transport in Poiseuille flow with a maximum velocity of v, an instantaneous injection at the inlet with a flux-weighted radial distribution of solute. An absorbing boundary condition is applied at the outlet, while reflecting boundary conditions are imposed for the inlet and the wall. Although the backward movement of tracer is possible (Aquino & Dentz 2018), its effect on hydrodynamic dispersion is minimal and, thus, ignored here. The PDF $\psi_t(t)$ for transition times through the tube is determined by the temporal evolution of solute flux at the outlet. We define the local Péclet number as $Pe_t = vR/D_m$ and the aspect ratio as $\eta = l/R$ with $\eta > 1$. The axial and radial diffusion times are denoted as $\tau_D = l^2/D_m$ and $\tau_{D,R} = R^2/D_m$, respectively. The transport through the tube can be categorised into three distinct modes, and approximate solutions for $\psi_t(t)$ can be derived for each mode (see the supplementary material).

Mode I occurs when $\tau < \tau_{D,R}$, where radial and axial diffusion are negligible. Particles move along streamlines with their transition times through the tube determined by advection. Thus, the distribution of transition times t is expressed as (see the supplementary material)

$$\psi_t(t) = 2\tau^2 t^{-3}. \tag{2.5}$$

However, molecular diffusion dominates within a layer near the wall due to no-slip condition. The thickness of this layer is estimated to be $\sqrt{2D_m\tau}$, the radial position of the layer is $r_B = R - \sqrt{2D_m\tau}$ and its corresponding velocity is $v_B = v(1 - r_B^2/R^2)$. It is assumed that tracers within this layer initially arrive at the boundary via diffusion and are subsequently transported by advection along the streamline to the outlet. Consequently, the transition time of the tracers within the layer is

$$\tau_B = \frac{l}{v_B} = \tau\sqrt{\frac{Pe_t}{8\eta}}. \tag{2.6}$$

Therefore, τ and τ_B set the lower and upper limits to the transition time, respectively. A simple derivation shows that the truncation time, $\tau_B \sim R^{-2}\sqrt{R^3/R^{-1}} \sim R^0$, is independent of R and constant for all conduits in mode I.

Mode II occurs when $\tau_{D,R} \leq \tau < \tau_D$. The solutes are fully mixed across the transverse direction, and the transition time distribution is strongly peaked near 2τ. Therefore, $\psi_t(t)$ is approximated by $\delta(t - 2\tau)$, where δ denotes the Dirac delta function.

Mode III occurs when $\tau \geq \tau_D$, that is, advection is slower than molecular diffusion, and $\psi_t(t)$ is approximately $\delta(t - \tau_D)$.

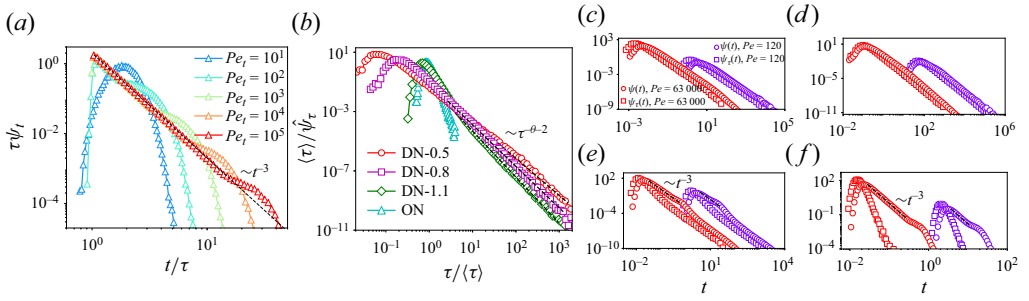

Figure 2. (*a*) PDF ψ_t of transition times through a tube with $\eta = 10$ for various local Péclet numbers Pe_t. The dashed line depicts the analytical solution for mode I, as described by (2.7). (*b*) Flux-weighted PDF $\hat{\psi}_\tau$ of advection times τ for the networks used in the simulation, including three disordered networks (DN-0.5, DN-0.8 and DN-1.1), which have large ratios of τ_{max}/τ_{min} and corresponding θ values of 0.5, 0.8 and 1.1, respectively, and one ordered network (ON), characterised by a small ratio of τ_{max}/τ_{min}. (*c*)–(*f*) The global PDF $\psi(t)$ of transition times (circles) compared with $\hat{\psi}_\tau(t)$ (squares) for (*c*) DN-0.5, (*d*) DN-0.8, (*e*) DN-1.1 and (*f*) ON. Here $\psi(t)$ exhibits a tail with the same power exponent of $-\theta - 2$ as $\hat{\psi}_\tau(t)$ for both (*c*) DN-0.5 and (*d*) DN-0.8, consistent with theoretical predictions for cases with a large τ_{max}/τ_{min} ratio and $0 < \theta < 1$. In contrast, $\psi(t)$ shows a heavier tail with a power exponent of -3, compared with $\hat{\psi}_\tau(t)$, for both (*e*) DN-1.1 and (*f*) ON, aligning with theoretical predictions for cases with either a small τ_{max}/τ_{min} ratio or $\theta > 1$.

Therefore, the shape of $\psi_t(t)$ is conditional on τ and thus we write

$$\psi_t(t \mid \tau) = \begin{cases} 2\tau^2 t^{-3} H(t-\tau) H(\tau_B - t), & \text{if } \tau < \tau_{D,R}, \\ \delta(t - 2\tau), & \text{if } \tau_{D,R} \le \tau < \tau_D, \\ \delta(t - \tau_D), & \text{if } \tau \ge \tau_D, \end{cases} \tag{2.7}$$

where H denotes the Heaviside function. These solutions are supported by random walk simulations (figure 2*a*).

The global PDF, $\psi(t)$, of tracer transition times is constructed as a weighted sum of the local PDFs, $\psi_t(t \mid \tau)$, for individual tubes, expressed as

$$\psi(t) = \frac{1}{N_0} \sum_{i=1}^{N_0} \frac{q_i}{\langle q \rangle} \psi_t(t \mid \tau_i) = \int_{\tau_{min}}^{\tau_{max}} \psi_t(t \mid \tau) \frac{q}{\langle q \rangle} \psi_\tau(\tau)\, \mathrm{d}\tau, \tag{2.8}$$

where N_0 represents the total number of tubes, and the subscript i indexes each tube. With (2.4), this expression is further simplified to the marginalisation of the joint PDF $\psi_t(t \mid \tau)\hat{\psi}_\tau(\tau)$ with respect to τ,

$$\psi(t) = \int_{\tau_{min}}^{\tau_{max}} \psi_t(t \mid \tau) \hat{\psi}_\tau(\tau)\, \mathrm{d}\tau. \tag{2.9}$$

The characteristics of $\psi(t)$ are shaped by the interplay between $\psi_t(t \mid \tau)$, which reflects intrapore flow variability, and $\hat{\psi}_\tau(\tau)$, which captures interpore flow variability. Here $\hat{\psi}_\tau(\tau)$ may vary significantly in terms of the exponent θ and the range of advection times τ_{max}/τ_{min}, modulated by α and R_{max}/R_{min}, respectively. Here, θ is constrained to be positive to ensure an asymptotic regime of constant dispersion.

3. Results and discussion

The expression for $\psi(t)$ is analysed separately for different values of τ_{max}/τ_{min} and θ, detailed derivations are provided in the supplementary material. From (2.2*a*,*b*), we

	$Pe_{c,3} < Pe < Pe_{c,2}$	$Pe_{c,2} < Pe < Pe_{c,1}$	$Pe > Pe_{c,1}$
Large τ_{max}/τ_{min}, $0 < \theta < 1$	$\langle t^2 \rangle \sim Pe^{-\theta-1}$	$\langle t^2 \rangle \sim Pe^{-2}$	$\langle t^2 \rangle \sim Pe^{-2}\ln(Pe)$
Large τ_{max}/τ_{min}, $\theta > 1$	$\langle t^2 \rangle \sim Pe^{-2}\ln(Pe)$	$\langle t^2 \rangle \sim Pe^{-2}\ln(Pe)$	$\langle t^2 \rangle \sim Pe^{-2}\ln(Pe)$
Large τ_{max}/τ_{min}, $\theta = 1$	$\langle t^2 \rangle \sim Pe^{-2}(\ln(Pe))^2$	$\langle t^2 \rangle \sim Pe^{-2}(\ln(Pe))^2$	$\langle t^2 \rangle \sim Pe^{-2}\ln(Pe)$
Small τ_{max}/τ_{min}			$\langle t^2 \rangle \sim Pe^{-2}\ln(Pe)$

Table 1. Leading-order behaviours of $\langle t^2 \rangle$ with Pe for networks with various τ_{max}/τ_{min} and θ, while $\langle t \rangle$ consistently follows $\langle t \rangle \sim Pe^{-1}$. A smaller θ value leads to a heavier tail in the distribution $\hat{\psi}_\tau(\tau)$. The ratio τ_{max}/τ_{min} represents the range of advection times, with large ratios of τ_{max}/τ_{min} estimated to be of the order of 10^2.

	$Pe_{c,3} < Pe < Pe_{c,2}$	$Pe_{c,2} < Pe < Pe_{c,1}$	$Pe > Pe_{c,1}$
Large τ_{max}/τ_{min}, $0 < \theta < 1$	$\frac{D_L}{D_m} \sim Pe^{-\theta+2}$	$\frac{D_L}{D_m} \sim Pe$	$\frac{D_L}{D_m} \sim Pe\ln(Pe)$
Large τ_{max}/τ_{min}, $\theta > 1$	$\frac{D_L}{D_m} \sim Pe\ln(Pe)$	$\frac{D_L}{D_m} \sim Pe\ln(Pe)$	$\frac{D_L}{D_m} \sim Pe\ln(Pe)$
Large τ_{max}/τ_{min}, $\theta = 1$	$\frac{D_L}{D_m} \sim Pe(\ln(Pe))^2$	$\frac{D_L}{D_m} \sim Pe(\ln(Pe))^2$	$\frac{D_L}{D_m} \sim Pe\ln(Pe)$
Small τ_{max}/τ_{min}			$\frac{D_L}{D_m} \sim Pe\ln(Pe)$

Table 2. Leading-order behaviours of D_L/D_m with Pe for networks with various τ_{max}/τ_{min} and θ. A smaller θ value leads to a heavier tail in the distribution $\hat{\psi}_\tau(\tau)$. The ratio τ_{max}/τ_{min} represents the range of advection times, with large ratios of τ_{max}/τ_{min} estimated to be of the order of 10^2.

derive the leading-order behaviours of $\langle t \rangle$ and $\langle t^2 \rangle$, which are summarised in table 1. Subsequently, the scaling relationships between D_L and Pe are determined from (2.1), as outlined in table 2.

For a large ratio of τ_{max}/τ_{min}, the transition modes throughout the network can be classified into three patterns based on Pe. We define $Pe_{c,1}$ and $Pe_{c,2}$ as the minimum Péclet numbers at which the conduit with τ_{max} reaches modes I and II, respectively, and $Pe_{c,3}$ as the minimum Péclet number for the conduit with τ_{min} as it reaches mode I. The expressions for $Pe_{c,1}$, $Pe_{c,2}$ and $Pe_{c,3}$ can be found in the supplementary material. When $Pe > Pe_{c,1}$, all conduits are in mode I. When $Pe_{c,2} < Pe < Pe_{c,1}$, conduits with smaller τ are in mode I, while those with larger τ are in mode II, separated by τ_0. Here, τ_0 denotes the maximum τ of tubes in mode I. When $Pe_{c,3} < Pe < Pe_{c,2}$, the conduits with the smallest to largest τ are in modes I, II and III, separated by τ_0 and τ_D, respectively. When $0 < \theta < 1$, $\hat{\psi}_\tau(\tau)$ dominates $\psi(t)$ for $t \leq \tau_{max}$, resulting in $\psi(t) \sim t^{-\theta-2}$, while $\psi_t(t \mid \tau)$ dominates for $\tau_{max} < t \leq \tau_B$, leading to $\psi(t) \sim t^{-3}$ (see the supplementary material), as illustrated in figure 2(*c*,*d*). When $\theta > 1$, $\psi_t(t \mid \tau)$ dominates $\psi(t)$ for $t \leq \tau_B$, resulting in $\psi(t) \sim t^{-3}$, while $\hat{\psi}_\tau(\tau)$ dominates for $t > \tau_B$, leading to $\psi(t) \sim t^{-\theta-2}$ (see the supplementary material), as depicted in figure 2(*e*). As Pe increases from $Pe_{c,3} < Pe < Pe_{c,2}$ to $Pe_{c,2} < Pe < Pe_{c,1}$ and, finally, to $Pe > Pe_{c,1}$, the scaling relationship transitions from $D_L/D_m \sim Pe^{2-\theta}$ to $D_L/D_m \sim Pe$ and, finally, to $D_L/D_m \sim Pe\ln(Pe)$ for $0 < \theta < 1$, whereas a consistent logarithmic scaling of $D_L/D_m \sim Pe\ln(Pe)$ is obtained for $\theta > 1$. For $\theta = 1$, the scaling relationship evolves from $D_L/D_m \sim Pe\ln^2(Pe)$ to $D_L/D_m \sim Pe\ln(Pe)$ as Pe increases.

For a small ratio of τ_{max}/τ_{min}, where $\hat{\psi}_\tau(\tau) \approx \delta(\tau - \tau_{min})$, tracer transitions predominantly occur in mode I. Thus, $\psi_t(t\,|\,\tau)$ dominates, leading to $\psi(t) = 2\tau_{min}^2 t^{-3}$ for $\tau_{min} \leq t < \tau_B$, as illustrated in figure 2(f). This behaviour leads to a logarithmic scaling of $D_L/D_m \sim Pe\ln(Pe)$.

The theoretical predictions are validated by experimental data on the dispersion coefficients of bead packs (Pfannkuch 1963) and by network simulations. Four networks are utilised in the simulation, including three disordered networks (DN-0.5, DN-0.8 and DN-1.1), which have large ratios of τ_{max}/τ_{min} and corresponding θ values of 0.5, 0.8 and 1.1, respectively, and one ordered network (ON), characterised by a small ratio of τ_{max}/τ_{min}, as depicted in figure 2(b). DN-0.8 is extracted from a monodisperse sphere pack whereas the other networks are artificially generated with a body-centred cubic lattice structure and varying pore size distributions. Since a monodisperse sphere pack closely replicates bead packs in dispersion experiments, DN-0.8 is employed to reproduce the experimental data. The reliability of the network model has been thoroughly confirmed by experimental data and direct numerical simulations (Liu *et al.* 2022, 2024*b*; please also see the supplementary material).

Network simulations based on DN-0.5 and DN-0.8 show a transition from $D_L/D_m \sim Pe^{2-\theta}$ to $D_L/D_m \sim Pe$ (figure 3). This observation supports theoretical predictions for cases with a large τ_{max}/τ_{min} ratio and $0 < \theta < 1$. The power exponents κ of the superlinear scaling are 1.5 and 1.2 for DN-0.5 and DN-0.8 (figure 3a), respectively, matching the theoretical prediction $\kappa = 2 - \theta$. Furthermore, $\kappa = 1.2$ of DN-0.8 aligns with experimental results (Sahimi 2011; Bear 2013). However, in the cases of DN-0.5 and DN-0.8, the scaling relationship $D_L/D_m \sim Pe\ln(Pe)$ is not observed, as achieving this scaling would require $Pe > 10^9$ (see the supplementary material), a threshold that arises from pronounced interpore flow variability and cannot be achieved under laminar flow conditions. Nonetheless, this does not preclude the possibility of observing this scaling in other media at more realistic, lower Pe.

The theoretical model indicates that the power-law regime is driven by significant interpore flow variability, which dominates the PDF of transition times and results in $\psi(t) \sim t^{-\theta-2}$. In narrow tubes, characterised by low flow velocities and large advective transition times, transport is diffusion-dominated for $Pe_{c,3} < Pe < Pe_{c,2}$, resulting in a truncated range of transition times spanning from τ_{min} to τ_D. Consequently, we obtain $\langle t\rangle \sim Pe^{-1}$ and $\langle t^2\rangle \sim Pe^{-\theta-1}$, and ultimately $D_L/D_m \sim Pe^{2-\theta}$ (see the supplementary material). This finding contrasts with prior studies (Koch & Brady 1985; Sahimi *et al.* 1986; Sahimi & Imdakm 1988; Jha *et al.* 2011; Mehmani & Balhoff 2015) that emphasise the importance of intrapore flow variability, typically linked to a logarithmic scaling relationship of $D_L/D_m \sim Pe\ln(Pe)$, which is closely approximated by $Pe^{1.2}$. However, this logarithmic term fails to explain the power-law regime of DN-0.5, which is characterised by a power exponent of 1.5. The limitation arises because $\ln(Pe)$ can only approximate Pe^a when a falls between 0.1 and 0.2, making it inadequate for more general cases where a varies. Thus, the logarithmic term does not offer a valid physical explanation for the power-law regime. For $Pe_{c,2} < Pe < Pe_{c,1}$, transport within the narrowest conduit changes to mode II, leading to transition times spanning from τ_{min} to τ_{max}, no longer truncated by τ_D. Thus, we get $\langle t\rangle \sim Pe^{-1}$ and $\langle t^2\rangle \sim Pe^{-2}$, and ultimately $D_L/D_m \sim Pe$ (see the supplementary material). The theory successfully predicts the transition from the power-law regime to the convective regime, a phenomenon not explained by previous theoretical models (Saffman 1959; Koch & Brady 1985; Bear & Bachmat 1986; Puyguiraud *et al.* 2021). A similar trend was obtained by Bijeljic & Blunt (2006) based on empirical PDFs of transition times, while our model offers the first theoretical

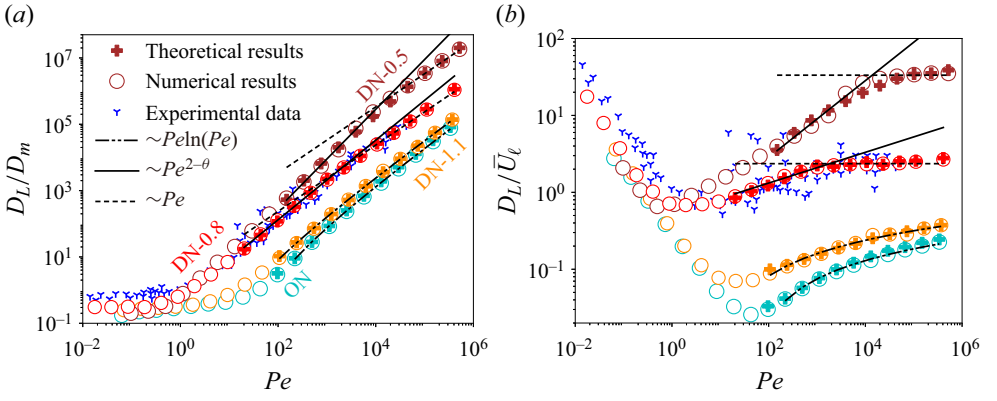

Figure 3. (*a*) Scaling relationships of D_L/D_m vs Pe for various networks, including three disordered networks, DN-0.5 (brown), DN-0.8 (red) and DN-1.1 (orange), which have large ratios of τ_{max}/τ_{min} and corresponding θ values of 0.5, 0.8 and 1.1, respectively, and one ordered network, ON (cyan), characterised by a small ratio of τ_{max}/τ_{min}. Theoretical results are derived from (2.1), where $\langle x\rangle = l\cos\beta$, and the moments $\langle t\rangle$ and $\langle t^2\rangle$ are calculated by (2.2*a*,*b*) using the PDF $\psi(t)$ given by (2.9). These theoretical predictions apply to hydrodynamic dispersion, where advection globally dominates transport. Numerical results are obtained through network simulations. The experimental data on the dispersion coefficients of bead packs (Pfannkuch 1963) are utilised to validate theoretical predictions and network simulations for DN-0.8. The global Péclet number is defined as $Pe = \bar{U}\ell/D_m$. (*b*) The relationship between $D_L/\bar{U}\ell$ (i.e. $D_L/D_m Pe$) vs Pe, using the same data and legends as in (*a*). Both DN-0.5 and DN-0.8 show a transition from $D_L/D_m \sim Pe^{2-\theta}$ to $D_L/D_m \sim Pe$, matching with the theoretical predictions for cases with a large τ_{max}/τ_{min} ratio and $0 < \theta < 1$. In contrast, both DN-1.1 and ON consistently follow the scaling $D_L/D_m \sim Pe\ln(Pe)$, in agreement with theoretical predictions for cases with either a small τ_{max}/τ_{min} ratio or $\theta > 1$.

confirmation. In contrast, network simulations indicate that hydrodynamic dispersion consistently follows a logarithmic scaling of $D_L/D_m \sim Pe\ln(Pe)$ for both DN-1.1 and ON, as shown in figure 3. This result aligns perfectly with the theoretical predictions for networks characterised by either a small τ_{max}/τ_{min} ratio or $\theta > 1$.

4. Conclusions

The theoretical model elucidates the scaling relationships between the hydrodynamic dispersion coefficient and the Péclet number across various porous media. We demonstrate that variations in structural disorder influence the relative significance of interpore vs intrapore flow variabilities, leading to distinct scaling behaviours. Specifically, in porous media characterised by a high ratio of τ_{max}/τ_{min} and $0 < \theta < 1$, the scaling behaviour transitions from $D_L/D_m \sim Pe^{2-\theta}$ to $D_L/D_m \sim Pe$, and eventually to $D_L/D_m \sim Pe\ln(Pe)$, as Péclet number increases. In contrast, when the ratio τ_{max}/τ_{min} is low or θ exceeds 1, a consistent logarithmic scaling of $D_L/D_m \sim Pe\ln(Pe)$ is observed. The power-law and linear scaling occur when interpore variability predominates over intrapore variability, while logarithmic scaling arises under the opposite condition. This framework provides valuable insights for modulating dispersion in porous media. Future research will aim to extend the framework to explore preasymptotic dispersion, a topic of broad interest (Di Federico & Neuman 1998; Dentz *et al.* 2004; Puyguiraud *et al.* 2021). Although the model primarily applies to hydrodynamic dispersion ($Pe > 1$), it can also be adapted to more complex flow conditions, such as multiphase flow and non-Newtonian flow.

Supplementary material. Supplementary material is available at https://doi.org/10.1017/jfm.2024.1131.

Funding. This work is financially supported by the NSF of China (grant numbers 12432013 and 12272207), National Key R&D Program of China (grant number 2019YFA0708704) and the Tsinghua University Initiative Scientific Research Program. M.D. acknowledges funding by the European Union through ERC grant KARST (project number 101071836). T.A. acknowledges financial support through the HydroPoreII project (PID2022-137652NB-C42), funded by MICIU/AEI/10.13039/501100011033 and ERDF/EU, and by the European Union (ERC Uplift 101115760).

Declaration of interests. The authors report no conflict of interest.

Author ORCIDs.
Tomás Aquino https://orcid.org/0000-0001-9033-7202;
Marco Dentz https://orcid.org/0000-0002-3940-282X;
Moran Wang https://orcid.org/0000-0002-0112-5150.

Author contributions. M.W. conceived and promoted this work. M.D. performed the theoretical derivations. Y.L. performed the simulations and theoretical derivations. Y.L. wrote the paper and M.W. revised the text. M.D., T.A. and H.X. performed the simulations and revised the text.

References

Acharya, R.C., van Dijke, M.I.J., Sorbie, K.S., Van der Zee, S.E.A.T.M. & Leijnse, A. 2007 Quantification of longitudinal dispersion by upscaling Brownian motion of tracer displacement in a 3D pore-scale network model. *Adv. Water Resour.* **30** (2), 199–213.

Alim, K., Parsa, S., Weitz, D.A. & Brenner, M.P. 2017 Local pore size correlations determine flow distributions in porous media. *Phys. Rev. Lett.* **119** (14), 144501.

de Anna, P., Le Borgne, T., Dentz, M., Tartakovsky, A.M., Bolster, D. & Davy, P. 2013 Flow intermittency, dispersion, and correlated continuous time random walks in porous media. *Phys. Rev. Lett.* **110** (18), 184502.

de Anna, P., Quaife, B., Biros, G. & Juanes, R. 2017 Prediction of the low-velocity distribution from the pore structure in simple porous media. *Phys. Rev. Fluids* **2** (12), 124103.

Aquino, T. & Dentz, M. 2018 A coupled time domain random walk approach for transport in media characterized by broadly-distributed heterogeneity length scales. *Adv. Water Resour.* **119**, 60–69.

Assouline, S., Tessier, D. & Bruand, A. 1998 A conceptual model of the soil water retention curve. *Water Resour. Res.* **34** (2), 223–231.

Bear, J. 2013 *Dynamics of Fluids in Porous Media*. Courier Corporation.

Bear, J. & Bachmat, Y. 1986 Macroscopic modelling of transport phenomena in porous media. 2. Applications to mass, momentum and energy transport. *Transp. Porous Media* **1**, 241–269.

Berkowitz, B., Cortis, A., Dentz, M. & Scher, H. 2006 Modeling non-Fickian transport in geological formations as a continuous time random walk. *Rev. Geophys.* **44** (2), RG2003.

Bijeljic, B. & Blunt, M.J. 2006 Pore-scale modeling and continuous time random walk analysis of dispersion in porous media. *Water Resour. Res.* **42** (1), 2005WR004578.

Bijeljic, B., Mostaghimi, P. & Blunt, M.J. 2011 Signature of non-Fickian solute transport in complex heterogeneous porous media. *Phys. Rev. Lett.* **107** (20), 204502.

Bijeljic, B., Muggeridge, A.H. & Blunt, M.J. 2004 Pore-scale modeling of longitudinal dispersion. *Water Resour. Res.* **40** (11), W11501.

Bizmark, N., Schneider, J., Priestley, R.D. & Datta, S.S. 2020 Multiscale dynamics of colloidal deposition and erosion in porous media. *Sci. Adv.* **6** (46), eabc2530.

Bruderer, C. & Bernabé, Y. 2001 Network modeling of dispersion: transition from Taylor dispersion in homogeneous networks to mechanical dispersion in very heterogeneous ones. *Water Resour. Res.* **37** (4), 897–908.

De Arcangelis, L., Koplik, J., Redner, S. & Wilkinson, D. 1986 Hydrodynamic dispersion in network models of porous media. *Phys. Rev. Lett.* **57** (8), 996–999.

Delgado, J.M.P.Q. 2005 A critical review of dispersion in packed beds. *Heat Mass Transfer* **42** (4), 279–310.

Dentz, M., Cortis, A., Scher, H. & Berkowitz, B. 2004 Time behavior of solute transport in heterogeneous media: transition from anomalous to normal transport. *Adv. Water Resour.* **27** (2), 155–173.

Dentz, M., Hidalgo, J.J. & Lester, D. 2023 Mixing in porous media: concepts and approaches across scales. *Transp. Porous Media* **146** (1-2), 5–53.

Dentz, M., Icardi, M. & Hidalgo, J.J. 2018 Mechanisms of dispersion in a porous medium. *J. Fluid Mech.* **841**, 851–882.

DENTZ, M., KANG, P.K., COMOLLI, A., LE BORGNE, T. & LESTER, D.R. 2016 Continuous time random walks for the evolution of Lagrangian velocities. *Phys. Rev. Fluids* **1** (7), 074004.

DI FEDERICO, V. & NEUMAN, S.P. 1998 Transport in multiscale log conductivity fields with truncated power variograms. *Water Resour. Res.* **34** (5), 963–973.

FATT, I. 1956 The network model of porous media. *Trans. AIME* **207** (1), 144–181.

GOIRAND, F., LE BORGNE, T. & SYLVIE, L. 2021 Network-driven anomalous transport is a fundamental component of brain microvascular dysfunction. *Nat. Commun.* **12** (1), 7295.

HUPPERT, H.E. & NEUFELD, J.A. 2014 The fluid mechanics of carbon dioxide sequestration. *Annu. Rev. Fluid Mech.* **46**, 255–272.

JHA, R.K., BRYANT, S.L. & LAKE, L.W. 2011 Effect of diffusion on dispersion. *SPE J.* **16** (1), 65–77.

JOHNSTON, P.R. 1998 Revisiting the most probable pore-size distribution in filter media: the gamma distribution. *Filtr. Separat.* **35** (3), 287–292.

JURTZ, N., KRAUME, M. & WEHINGER, G.D. 2019 Advances in fixed-bed reactor modeling using particle-resolved computational fluid dynamics (CFD). *Rev. Chem. Engng* **35** (2), 139–190.

KANDHAI, D., HLUSHKOU, D., HOEKSTRA, A.G., SLOOT, P.M., VAN AS, H. & TALLAREK, U. 2002 Influence of stagnant zones on transient and asymptotic dispersion in macroscopically homogeneous porous media. *Phys. Rev. Lett.* **88** (23), 234501.

KOCH, D.L. & BRADY, J.F. 1985 Dispersion in fixed beds. *J. Fluid Mech.* **154**, 399–427.

LEHOUX, A.P., RODTS, S., FAURE, P., MICHEL, E., COURTIER-MURIAS, D. & COUSSOT, P. 2016 Magnetic resonance imaging measurements evidence weak dispersion in homogeneous porous media. *Phys. Rev.* E **94** (5), 053107.

LIU, Y., GONG, W., XIAO, H. & WANG, M. 2024*a* Non-monotonic effect of compaction on longitudinal dispersion coefficient of porous media. *J. Fluid Mech.* **988**, R2.

LIU, Y., GONG, W., XIAO, H. & WANG, M. 2024*b* A pore-scale numerical framework for solute transport and dispersion in porous media. *Adv. Water Resour.* **183**, 104602.

LIU, Y., GONG, W., ZHAO, Y., JIN, X. & WANG, M. 2022 A pore-throat segmentation method based on local hydraulic resistance equivalence for pore-network modeling. *Water Resour. Res.* **58** (12), e2022WR033142.

MAIER, R.S., KROLL, D.M., BERNARD, R.S., HOWINGTON, S.E., PETERS, J.F. & DAVIS, H.T. 2000 Pore-scale simulation of dispersion. *Phys. Fluids* **12** (8), 2065–2079.

MEHMANI, Y. & BALHOFF, M.T. 2015 Eulerian network modeling of longitudinal dispersion. *Water Resour. Res.* **51** (10), 8586–8606.

MOSTAGHIMI, P., BIJELJIC, B. & BLUNT, M.J. 2010 Simulation of flow and dispersion on pore-space images. *SPE J.* **17** (4), 1131–1141.

PENG, X., KULKARNI, D., HUANG, Y., OMASTA, T.J., NG, B., ZHENG, Y., WANG, L., LAMANNA, J.M., HUSSEY, D.S. & VARCOE, J.R. 2020 Using operando techniques to understand and design high performance and stable alkaline membrane fuel cells. *Nat. Commun.* **11** (1), 3561.

PFANNKUCH, H.O. 1963 Contribution a l'etude des deplacement de fluids miscible dans un milieu poreux. *Rev. Inst. Fr. Petrol.* **18** (2), 215–270.

PUYGUIRAUD, A., GOUZE, P. & DENTZ, M. 2021 Pore-scale mixing and the evolution of hydrodynamic dispersion in porous media. *Phys. Rev. Lett.* **126** (16), 164501.

SAFFMAN, P.G. 1959 A theory of dispersion in a porous medium. *J. Fluid Mech.* **6** (3), 321–349.

SAHIMI, M. 2011 *Flow and Transport in Porous Media and Fractured Rock: From Classical Methods to Modern Approaches*. John Wiley & Sons.

SAHIMI, M., HUGHES, B.D., SCRIVEN, L.E. & DAVIS, H.T. 1986 Dispersion in flow through porous media – I. One-phase flow. *Chem. Engng Sci.* **41** (8), 2103–2122.

SAHIMI, M. & IMDAKM, A.O. 1988 The effect of morphological disorder on hydrodynamic dispersion in flow through porous media. *J. Phys.* A*: Math. Gen.* **21** (19), 3833.

SAHIMI, M. & IMDAKM, A.O. 1991 Hydrodynamics of particulate motion in porous media. *Phys. Rev. Lett.* **66** (9), 1169.

VAN MILLIGEN, B.P. & BONS, P.D. 2014 Simplified numerical model for clarifying scaling behavior in the intermediate dispersion regime in homogeneous porous media. *Comput. Phys. Commun.* **185** (12), 3291–3301.